ADVANCED MATERIALS
www.advmat.de

Fast and Efficient Fabrication of Functional Electronic Devices through Grayscale Digital Light Processing 3D Printing

*Farzad Gholami, Liang Yue, Mingzhe Li, Ayush Jain, Akhlak Mahmood, Marcus Fratarcangeli, Rampi Ramprasad, and H. Jerry Qi**

Fabricating polymeric composites with desirable characteristics for electronic applications is a complex and costly process. Digital light processing (DLP) 3D printing emerges as a promising technique for manufacturing intricate structures. In this study, polymeric samples are fabricated with a conductivity difference exceeding three orders of magnitude in various portions of a part by employing grayscale DLP (g-DLP) single-vat single-cure 3D printing deliberate resin design. This is realized through the manipulation of light intensity during the curing process. Specifically, the rational resin design with added lithium ions results in the polymer cured under the maximum UV-light intensity exhibiting higher electrical resistance. Conversely, sections that are only partially cured retains uncured monomers, serving as a medium that facilitates ion mobility, consequently leading to higher conductivity. The versatility of g-DLP allows precise control of light intensity in different regions during the printing process. This characteristic opens up possibilities for applications, notably the low-cost, facile, and rapid production of complex electrical circuits and sensors. The utilization of this technique makes it feasible to fabricate materials with tailored conductivity and functionality, providing an innovative pathway to advance the accelerated and facile creation of sophisticated electronic devices.

1. Introduction

Polymeric conductors, with their distinctive attributes of stability,[1] biocompatibility, and favorable electrical and mechanical properties,[2] find applications in diverse fields such as energy storage,[3] flexible electronics,[4] and bioelectronics.[5] In recent years, researchers have shown a keen interest in additive manufacturing (AM) of soft electronics.[6] A common technique in this field is to manufacture 3D objects using conductive polymers[7] (such as poly(3,4-ethylenedioxythiophene)-poly(styrenesulfonate)(PEDOT:PSS)) or hydrogels containing conductive materials such as metallic conductors,[8] intrinsically conductive polymers,[9] and carbon-based materials[9b,10] (carbon nanotubes, carbon nanoparticles, etc.). However, these methods have limitations. Objects 3D printed with pure conductive polymers are brittle,[11] moreover materials printed with this approach exhibit uniform conductivity throughout the entire object. These drawbacks restrict the capability of this approach in fabricating complex and functional devices. Achieving functional electronic components through these methods often requires multistep manufacturing processes and assembly, leading to a significant increase in process complexity and reduction in efficiency.

Functional and complex soft electronics require different levels of conductivity in different regions of a part to create conductive paths. For example, a strain sensor typically consists of a conductive trace embedded in a nonconductive matrix. In the AM field, the predominant techniques for fabricating soft electronics involve printing conductive traces using highly conductive materials such as silver,[12] gold,[13] and intrinsically conductive polymers (e.g., PEDOT:PSS,[14] polypyrrole[15]) on a flexible and non-conductive substrate.[6c,7a,12,16] Generally, these traces are printed in thin layers to maintain the flexibility of the overall structure, considering the stiffness of metallic conductors[12,13] and the brittle nature of the conductive polymers.[11a,17] Despite the fabrication of flexible electronics using 3D printing techniques, conductive materials are generally printed in a 2D plane. Vias are then added if conductive traces in different planes

F. Gholami, L. Yue, M. Li, M. Fratarcangeli, H. J. Qi
The George W. Woodruff School of Mechanical Engineering
Georgia Institute of Technology
Atlanta, GA 30332, USA
E-mail: qih@me.gatech.edu
F. Gholami, A. Jain, A. Mahmood, R. Ramprasad, H. J. Qi
School of Materials Science and Engineering
Georgia Institute of Technology
Atlanta, GA 30332, USA
A. Jain
College of Computing
Georgia Institute of Technology
Atlanta, GA 30332, USA

The ORCID identification number(s) for the author(s) of this article can be found under https://doi.org/10.1002/adma.202408774

DOI: 10.1002/adma.202408774

need to be connected.[18] Additionally, the mechanical properties mismatch between the flexible substrate and the conductive materials poses a challenge,[17b,19] limiting the ability to construct complex 3D objects. Another approach involves fabricating intricate structures and designing desired circuits as hollows within the polymeric structure. After the printing process, these hollows can be filled with conductive materials such as liquid metals to establish conductivity.[20] Various AM methods, such as digital light processing (DLP), direct ink writing (DIW), and inkjet printing (IJP), can be employed for this purpose. Another strategy for fabricating complex polymeric electronics involves using hybrid printing by combining different 3D printing techniques. For example, the combination of DIW and DLP is a common hybrid 3D printing approach for multimaterial 3D printing.[21] Peng et al.[21b] introduced a hybrid DLP/DIW printer for in situ printing of conductive inks with DIW in high resolution and complex structures printed with DLP. While this technique exhibits promising results in manufacturing complex conductive structures, it has drawbacks, including slow production rates and the necessity of complicated setups.[22] Additionally, the properties mismatch between the two materials printed with DLP and DIW poses a challenge to the structural integrity of the objects.[22] Another prevalent multilateral 3D printing method is multi-nozzle DIW, which involves multiple nozzles containing different inks and dispenses them on demand for fabricating complex objects.[23] This technique enables the production of complex conductive electronics.[23b] However, it is associated with some critical challenges. In this method, the inks from different nozzles should exhibit similar flow behavior to meet printing demands. Adjusting printing parameters such as extrusion speed for each nozzle, temperature, start/stop times, etc., poses a significant challenge. Moreover, the adhesion between layers is also a limiting factor.[24] A different strategy for manufacturing complicated conductive structures through 3D printing involves using multi-vat DLP, as reported by Mu et al.[25] In this approach, objects are printed in two separate vats-one containing conductive ink and the other non-conductive ink. Consecutive curing of the resins provides the opportunity to fabricate multimaterial objects with complex structures and desired conductive circuits alongside a non-conductive matrix. While this technique allows for the creation of super complex conductive objects, there are limitations due to the intermittent resin exchange mechanism, requiring extensive cleaning.[26] The process is time-consuming, and even automated processes may not ensure complete cleaning during swapping between multiple vats.[27] Moreover, issues such as interlayer adhesion, anisotropic properties, and the incompatibility of multiple polymers often result in poor material properties and premature damage to the printed objects.[27a]

Grayscale DLP (g-DLP) 3D printing stands out as a promising solution in AM enabling us to address the challenges outlined earlier associated with other 3D printing methods for fabrication of soft electronics. G-DLP represents a modified iteration of DLP 3D printing designed for the seamless fabrication of multimaterial in a single vat and a single 3D printing process, eliminating the need for additional steps.[20b,28] This technique operates by manipulating the light intensity of the projector through the adjustment of the brightness in different regions in a cross section image, a departure from the black and white slides employed in conventional DLP.[28a] Varying light intensity during the DLP process results in changing degrees of monomer conversion.[20a,28a] This nuanced control significantly influences the final properties of the 3D printed objects. The efficacy of this approach has been demonstrated in successfully producing materials with target mechanical properties[20,28a] and distinct colors,[29] but for conductive structures.

In this study, leveraging the advanced capabilities of g-DLP 3D printing and designing a resin with specific properties, we introduce an approach for manufacturing complex yet fully functional soft electronics. Here, lithium ions served as the source of charge centers. In the process of printing the resin containing lithium ions, sections exposed to higher intensity light exhibit increased cross-linking, whereas those cured under lower light intensity show low monomer conversion. This disparity in cross-linking degree significantly impacts the variation in ion mobility across the sample, thereby resulting in distinct conductivities within different sections. Through systematic study, we design the DLP ink that offers the possibility to achieve varying levels of conductivity by precisely controlling the light intensity during the DLP 3D printing process. The conductivity and glass transition temperature (T_g) measurements are verified by molecular dynamic (MD) simulations; the established simulation protocol may serve future accelerated device design efforts by augmenting and guiding experimental efforts. Samples, in their as-printed state, exhibit conductivity differences of up to 2000 times (2×10^{-2} vs 1×10^{-5} S m^{-1}) in various sections. This notable contrast in conductivity is achieved solely by adjusting the curing light intensity in the DLP process, without changing any other parameters during 3D printing. Consequently, we can produce samples with a wide range of conductivity levels for diverse applications. The samples exhibit full functionality post-printing, eliminating the need for additional steps or post-processing. Given the inherent characteristics of g-DLP, particularly its single-vat, single-print nature, this process is highly efficient, enabling the fast production of intricate electronics and circuits within minutes. This opens avenues for the fabrication of complex and highly functional electronics without necessitating changes to printer parameters, but only to the slides employed.

2. Results

2.1. Material Characterization and Properties

The rationally designed resin as shown in **Figure 1a** contains glycidyl methacrylate (GMA) as the linear chain builder, poly(ethylene glycol) diacrylate (PEGDA) as the cross-linker and reactive diluent, and aliphatic urethane diacrylate (AUD) as the cross-linker, photo-initiator (PI819), and photo-absorber (Sudan I). Our resin also contains lithium salt, lithium bis(trifluoromethanesulfonyl)imide (LiTFSI), as a charge transfer agent and source of electrical conductivity. In g-DLP, the light intensity is a parameter that controls the monomer conversion at different regions of the printed samples. Higher light intensity during photopolymerization results in a high degree of conversion (DoC),[30] that yields a polymer network that is extensively cross-linked. Conversely, a lower intensity light creates a network with a low DoC, which preserves a phase that contains lower molecular weight chains and less cross-linked structure (Figure 1b). The presence of this phase

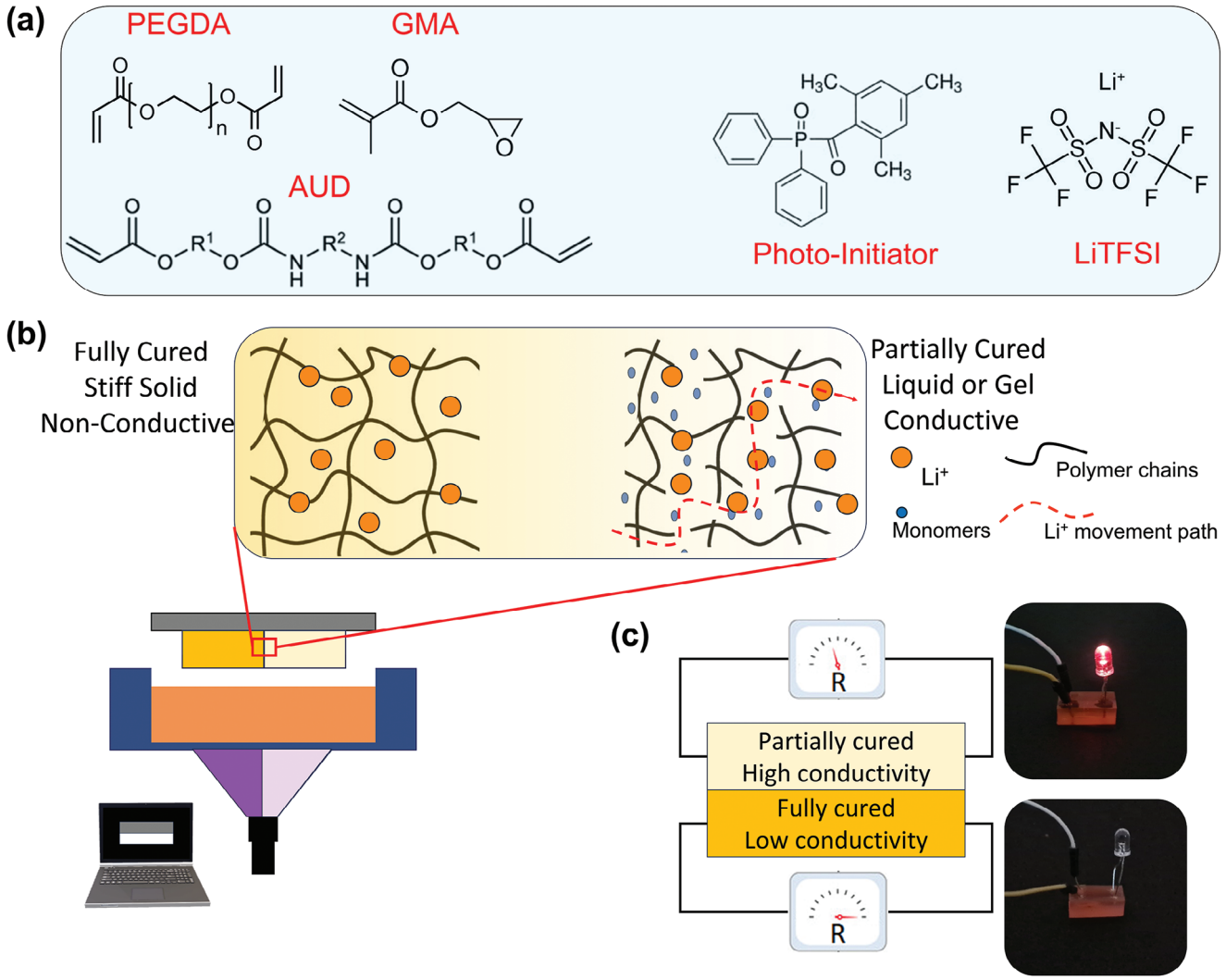

Figure 1. Illustration of single-vat DLP 3D printing for conductive materials. a) Chemical structure of the resin components, b) schematic illustration of the cross-linked structure in polymer due to light intensity differences in g-DLP 3D printing. c) Different conductivity observed in the printed samples with different light intensities.

creates a medium[31] facilitating the mobility of lithium ions and allowing for their movement through the polymer matrix. Therefore, regions printed with lower light intensity, which is associated with a lower DoC, exhibit higher electrical conductivity in comparison to regions subjected to higher light intensity. The controlling DoC by light intensity provides the opportunity to achieve different levels of ionic conductivity across different part of the printed samples via g-DLP technique (Figure 1c).

We measure the conductivity of phases by creating a channel with different light intensities within a bulk material with maximum light intensity (G0), calculating conductivity by measuring the resistance at both ends (**Figure** 2a). In this study G0 is denoted as the maximum light intensity and G100 corresponds to light off, (detailed information of all grayscales used throughout the project and their corresponding light intensities are presented in Table S1, Supporting Information). The conductivity of samples with high degree of conversion (grayscales smaller than G60), which are in solid form, is measured using a four-point probe conductivity instrument from a printed polymer sheet of the resin (Figure 2a). Figure 2b illustrates the conductivity versus LiTFSI concentration in G80 channels printed in G0 matrix as well as the ratio between the conductivity of G80 and G0. It could be observed that conductivity increases with LiTFSI concentration up-to 20 wt%, while it reaches a plateau in higher concentrations. However, at higher concentration of the lithium ions in the matrix decreases the ratio of G80/G0 conductivity, this is because of the increase in the conductivity of the G0 in higher lithium ions concentrations. Therefore, in the rest of this paper 20 wt% LiTFSI salt is used. Figure 2c shows the conductivity versus grayscale in printed samples. It can be observed that by moving from G100 toward G0, the conductivity decreases in three different regions. The first region is the grayscales where there is not enough light intensity to make a cross-linked structure, consequently the resin is still in liquid phase. In grayscales smaller than G80 (increasing light intensity) the conductivity drops after passing the gel point, due to the decrease of the mobility of

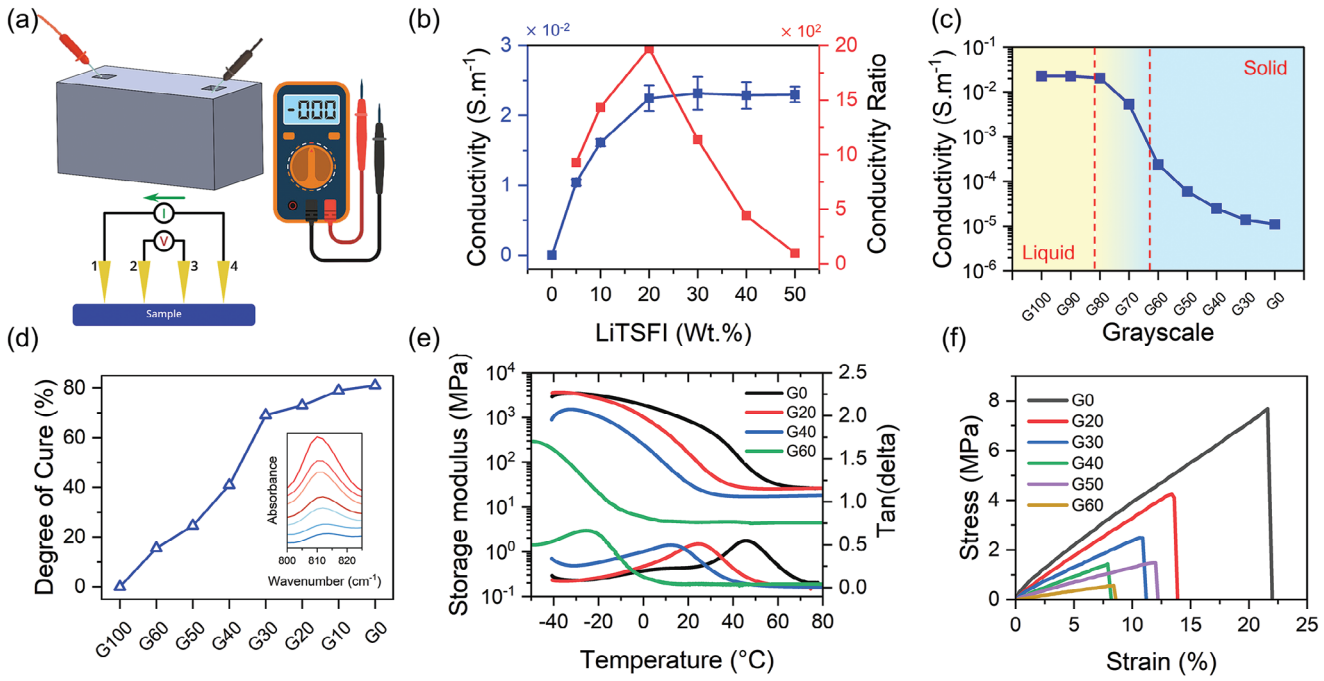

Figure 2. Basic properties of the printed samples. a) schematic representation of measuring the resistance of the liquid and solid samples, b) the conductivity of the resin in different LiTSFI ion concentration as well as the ratio of conductivity of G0/G80, c) the conductivity of the printed samples in different grayscales, d) DoC curve versus different grayscales obtained from FTIR analysis, e) storage modulus and tan δ as a function of temperature for the g-DLP printed samples, f) stress-strain curves of G60 to G0.

lithium ions. By decreasing the grayscale (higher light intensity), the conductivity drops more and lower than G60 the cross-linking density is high enough for formation of near glassy polymers. It can be observed that by controlling the light intensity in g-DLP, we are able to achieve a wide range of conductivity that has up to 2000-fold difference in conductivity, when G0 is compared with samples ≥ G80. Also, even in solid state samples, the conductivity of G60 is 20 times higher than G0. In this system, the conductivity is primarily facilitated by the movement of lithium ions. In the partially cured state, the polymer chains remain sufficiently mobile to allow for the transport of lithium ions, which are the primary charge carriers. This mobility is crucial for maintaining ionic conductivity. The gel-state provides an environment where the ions can move through the resin matrix with relative ease, unlike in a fully cured, rigid matrix where ionic transport would be significantly restricted. The polymer chain mobility and thus viscosity of the matrix plays a key role in lithium ion mobility. Lower cross-linking density results in chains remaining flexible and lower viscosity. Both enable easier movement of ions through the matrix. Conversely, higher cross-linking density reduces polymer chain flexibility and increases viscosity, which in turn restricts ion movement. In highly cross-linked systems, the rigid polymer chains impede lithium ion transport, leading to reduced conductivity. This mechanism is further supported by the inherent properties of ion-conductive gels, where ionic conductivity is achieved through the dissociation of lithium salts and the subsequent transport of lithium ions facilitated by the polymer chains' flexibility in the gel state. Studies have shown that the ionic conductivity in such systems can be attributed to both the segmental motion of the polymer chains and the presence of free ions that migrate under an electric field.[32] Our MD simulations further confirm this mechanism, which in the next section will be elaborated.

This study introduces a grayscale DLP single-vat and single-cure 3D printing method capable of producing parts with a conductivity range of 10^{-2} to 10^{-5} S m^{-1} using 20 wt% lithium salt. Although this range may fall short for high-performance circuit applications, the method excels in rapid prototyping, providing a streamlined process for developing functional electronic components. This moderate conductivity contrast achieved is sufficient for several applications, including soft robotics, flexible sensors, and biomedical devices. Moreover, this range of conductivity has been successfully employed in other studies for circuit printing, highlighting its practical applicability in certain contexts.[25,33] The simplicity of this approach allows for efficient design testing and iteration before committing to more demanding fabrication techniques. Continued research is directed toward optimizing the conductivity and insulation levels, with the goal of expanding the utility of this method in advanced 3D printing applications.

Figure 2d shows the DoC of the samples in different grayscale calculated via monitoring the intensity of the C=C bond at ≈810 cm^{-1} with respect to carbonyl group peak at ≈1720 cm^{-1} as reference. The absorbance peak of the samples in different grayscale are shown in Figure S1 (Supporting Information). As expected, the higher light intensity results in higher DoC. We further evaluate thermomechanical properties of the samples with dynamic mechanical analyses (DMA), as shown in Figure 2e. The glass transition temperature (T_g) of the samples increases by increasing the light intensity, from −6 °C for G60 to 40 °C

for G0. Figure 2f displays the strain-stress behaviors obtained from the uniaxial tensile tests. The Young's modulus of the samples increases from 8 to 60 MPa for G60 and G0, respectively. It is important to note that although the mechanical properties of the partially cured parts are relatively low, our design strategically combines fully cured and partially cured sections. The fully cured parts, positioned adjacent to the partially cured regions, provide the necessary mechanical strength for specific applications. This approach ensures that the overall mechanical properties are maintained and not compromised by the conductive regions with relatively weak mechanical properties. By carefully integrating these sections, we achieve a balance that preserves the structural integrity while allowing for high conductivity where needed. The variations of the conduction, thermal, and mechanical properties as a function of starting materials, their compositions, curing conditions, and LiTFSI concentration reveal the staggering breadth of the design space that is available for optimization. Efficiently and effectively exploring this design space offers a fertile ground for future innovations in this field.

2.2. Molecular Dynamics Simulations

One way to efficiently explore this chemical and environmental space is through simulations. As a first step in that direction, here, the polymer structures in different grayscale (monomer conversion) are evaluated via MD simulations to verify the conductivity and glass transition temperature in this system. **Figure 3a** shows the snapshot of the molecules in the MD simulations at 0, 40, and 80% conversion of monomers. The glass transition temperature of the samples in the simulation is obtained via measuring the density of the samples during temperature sweep tests. The density versus temperature relationship has distinct slopes at temperatures below and above the T_g, and the T_g is the temperature at the intersection of these two linear regions. Figures S2 and S3 (Supporting Information) presents the density versus temperature graphs for two curing stages, 10% and 80%, respectively. To evaluate a few suitable atomic-level representations of thermoset systems (for a given degree of cross-linking) amenable to MD simulations, we adopted three methods to create small models of cross-linked systems and the evaluated the resulting simulated values of T_g. The first method, visualized in Figure 3b for an 80% cured system, was composed of clustered subsystems with cross-links within the subsystems only, i.e., there were no cross-links between clusters or across periodic boundary conditions (although bonds along the monomer chains persist). The second method, visualized in Figure 3c, maintained the full 3D network structure of the thermoset by allowing cross-links between cluster subsystems and across the periodic replicas. This created a stiff thermoset network that spans across periodic boundaries. The third method is intermediate to the first and second methods, where the small subsystems are connected inside the periodic boundary box, but no cross-links go across the periodic boundaries. This is meant to give the system more freedom to move, while maintaining the cross-linked nature of the bulk material. Evaluating such varied cross-linking architectures is essential to get a better sense of statistical variations in results, especially given that it is not a priori clear what the correct cross-linked morphology occurs in the experimental systems for a given DoC.

The simulations are repeated for various DoCs, and the results are compared with experimental data obtained from DMA in Figure 3d. Both the experimental and simulation results exhibit a similar trend, albeit with some margin of error. The system built with clustered smaller systems adheres the most closely to the experimentally obtained T_g values. The systems using both the periodic and non-periodic thermoset networks are shown to have higher T_g values than what is experimentally observed. All models though display the correct qualitative trend of increasing Tg with increasing DoC, with roughly the right slope relative to experiments.

The lithium-ion conductivity was simulated for the first model (i.e., the small clustered systems) of cross-linked polymers. Figure 3e shows the conductivity as a function of DoC and compares these results with experimental measurements. While we do not see a quantitative agreement with experiments, the qualitative trend of decreasing conductivity with increasing DoC is indeed borne out by the simulations. As shown in Figure 3a, the simulations demonstrate that cross-linking limits the chain mobility of the monomers. Figure 3f further visualizes the cross-linking effects on the LiTFSI ion pair. At 0% cure, a polymer network backbone has not formed, and allows for the monomers surrounding LiTFSI to move. At 80% cure, the network structure has formed, restricting the motion of surrounding segments and thereby influencing the ion transport in cross-linked polymer systems. We note that in this case with dual-ion conduction, $TFSI^-$ and Li^+ ions are found to move together. Because $TFSI^-$ is a large molecule, the restrictions on ion transportation further limits its motion, causing pronounced decreases in Li^+ ion transport. The discrepancies with experiments primarily arise from the use of a small cross-linked polymer network model, the challenges with classical force fields to simulate cross-linked and ion-containing systems, and lack of clear knowledge on the morphology of the cross-linked system. Nonetheless, the ability of such classical MD simulations to capture the correct trends in at least a semi-quantitative manner opens up opportunities to utilize a combination of a small high-fidelity experimental dataset with a large lower-fidelity simulation dataset within a multi-task machine learning framework to build high-quality predictive models.

2.3. g-DLP 3D Printing of Electrical Circuits

To showcase the capabilities and robustness of the combination of our resin and g-DLP 3D printing, we fabricate various electrical circuits within the single vat, single resin 3D printing process. Importantly, these circuits are employed in their as-printed state, requiring no further modifications or post-processing procedures. To accomplish this, we leverage the difference in conductivity (up to 2000-fold) between fully cured sample (G0) and the samples on the other end of spectrum of conversion (>G80). This significant difference in conductivity enables us to form conductive traces (or channels printed with G80) intricately embedded within complex structures, despite the matrix structures exhibiting substantially lower conductivity (printed with G0). The material in the channels is printed with G80 grayscale since at this light intensity the resin forms a viscous liquid as it is near the gel point, preventing it from flowing easily while the conductivity is comparable with uncured resin (G100).

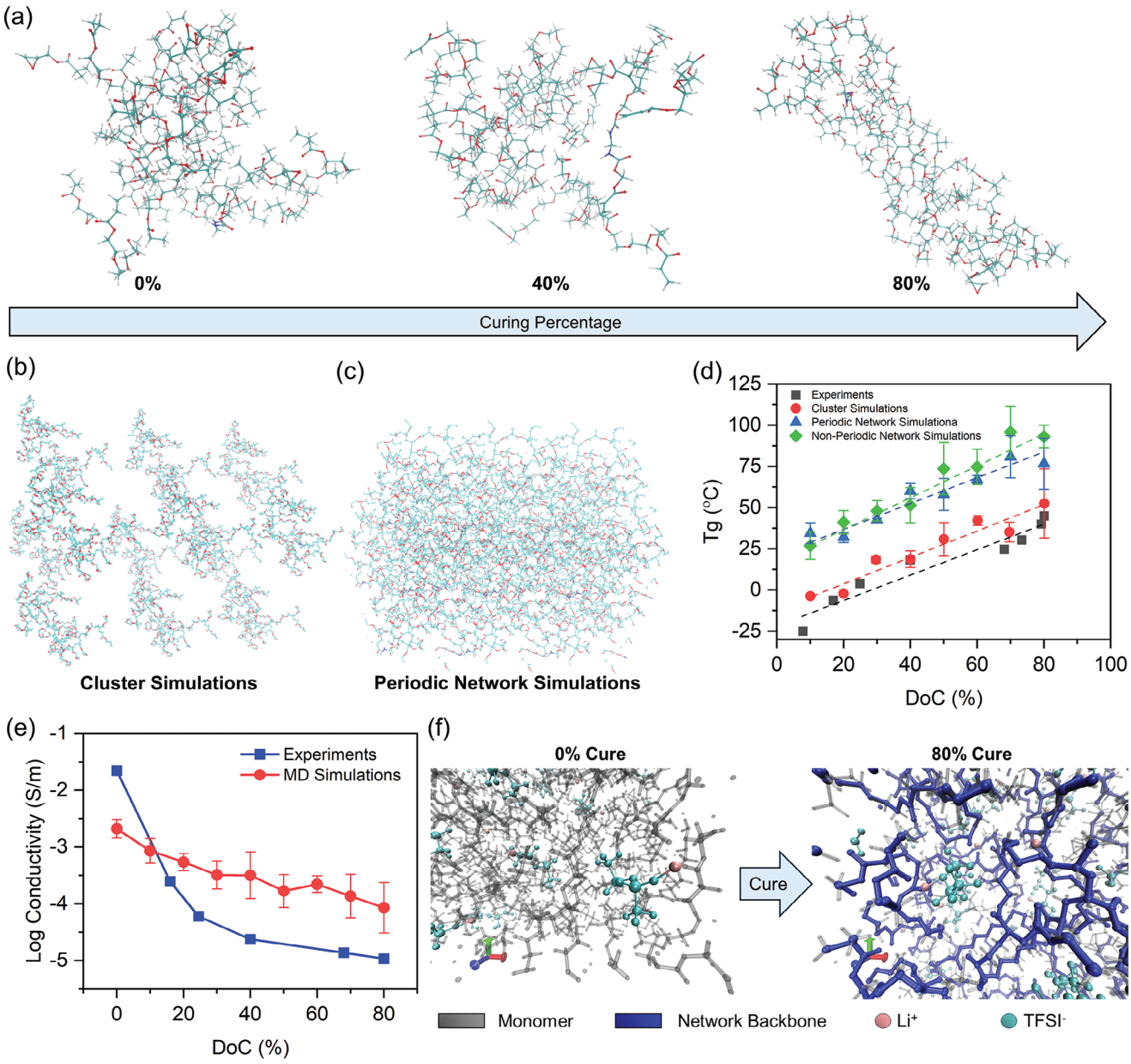

Figure 3. The results of MD simulation of this system. a) Snapshot of molecules in MD simulation process at different curing percentages; 0, 40, and 80%. b) An example system of 80% curing when treating the system as smaller cross-linked clusters. c) An example system of 80% curing when treating the system as a periodic network. d) Comparison of glass transition temperature in experiments a and MD simulations. e) The comparison between conductivity obtained from experiments and MD simulations. f) The mechanism of LiTFSI ion interactions with the monomer system at 0% cure with no network backbone formation and at 80% cure with network formation.

In **Figure** 4a, we present a simplified circuit prototype, wherein two G80 (2×10^{-2} S m^{-1}) channels are discretely embedded (denoted with red color) within a rectangular prism constructed with G0 (1×10^{-5} S m^{-1}) material. The dimension of the conductive trace inside the matrix is 2×2 mm with 10 mm length. These channels serve as efficient conductive traces and an LED diode is connected to the opposite terminus. When a 15 V voltage is applied to one end, the diode illuminates without encountering any short-circuiting issues, demonstrating the successful functionality of the system. This configuration underscores the promising potential of the combination of proper material and 3D printing technique to achieve advance parts for electronic applications. Our material exhibits consistent conductivity in our circuit experiment. To illustrate this, we monitor the light intensity of the diode while it is connected. Figure S4 (Supporting Information) shows the LED diodes at various time intervals. The diode's light output remains virtually unchanged even after a duration of 2 h, indicating stable conductivity. This observation indicates the reliability of our material in sustaining conductivity over extended periods, a critical attribute in various practical applications.

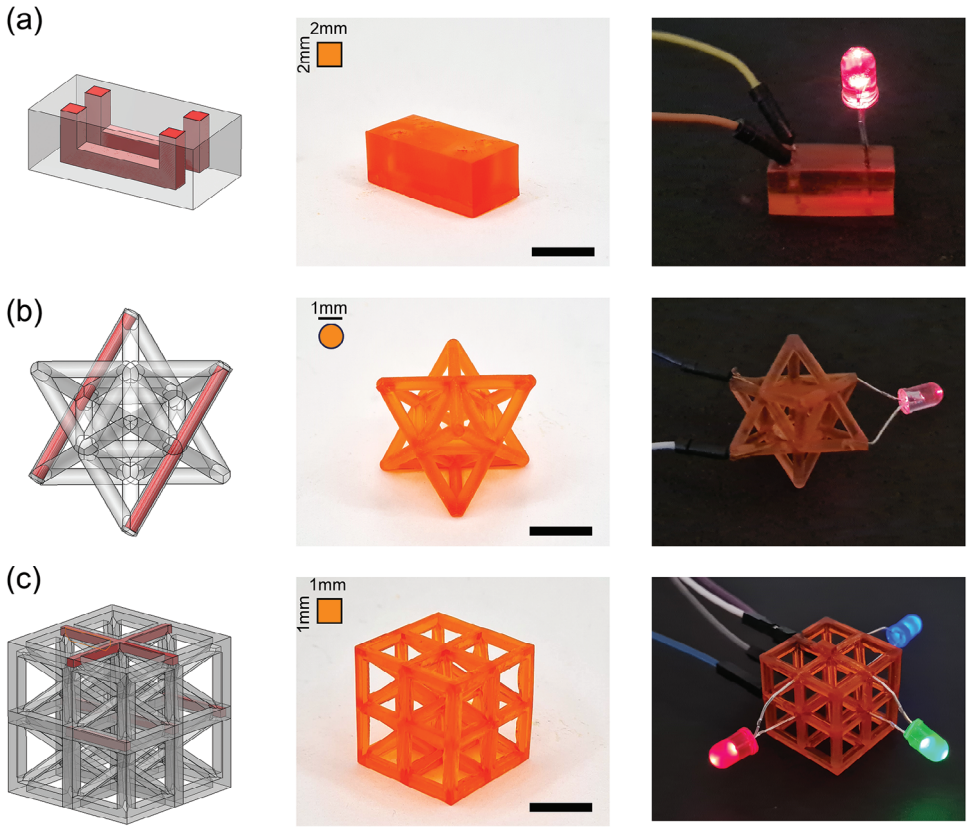

Figure 4. Printed circuits with g-DLP with different configurations. a) Schematic illustration and image of printed block with integrated channels imbedded inside, printed with low light intensity that can act as wires to light-up led. b) Complex circuits printed in lattice structures. d) Printing of multiple district conductive traces embedded in a lattice structure to light-up different LEDs separately. The scale bar is 10 mm.

This approach can be readily extended to produce intricate circuits with a high degree of complexity. For instance, as illustrated in Figure 4b, we 3D print a more complex structure housing two embedded conductive traces capable of illuminating LED diodes. This is a single unit-cell of a lattice where two conductive traces are designed inside two edges of the structure (red color parts). The cross section of these polymeric wires is circular with diameter of 1 mm and length of 20 mm. Remarkably, this particular sample is printed in an efficient 25 min and is fully operational right after printing. The technique can be elevated to the next level by introducing multiple conductive pathways within intricate structures, enabling the creation of advanced circuits with diverse functionalities. Figure 4c and supplementary Movie S1 (Supporting Information) show the integration of multiple channels within a complex lattice structure to simultaneously illuminate distinct LED diodes. In the design in Figure 4c, there are four separate conductive traces. One of them (the one with cross shape at the top of the model) is shared among all three LEDs and connects their positive end to the power source. On the other hand, separate channels are designed for connecting the negative end of LEDs to the power sources. This sample is printed in only 18 min and provides the capabilities to control the LED diodes separately. The channels cross section dimensions are 1 × 1 mm. This lattice structure enables us to effectively illuminate multiple diodes where each LED can be controlled separately by designing discrete channels embedded inside the structure. This capability empowers us to 3D print electrical circuits of varying complexities tailored for a wide spectrum of applications. It is noteworthy that this technique can be extended to other ink formulations, as demonstrated in Figure S5 (Supporting Information), where we successfully 3D printed circuits using butyl acrylate (BA), PEGDA, and AUD with a weight ratio of 45:45:10 (BA:PEGDA:AUD). Additionally, we utilized 2-hydroxyethyl acrylate (2-HEA) and Bisphenol A ethoxylate diacrylate (BPAEDA) with a weight ratio of 80:20 (2-HEA:BPAEDA). The concentrations of LiTFSI, PI819, and Sudan I in these inks are consistent with those used in the primary ink formulation for the remainder of this study.

A potential concern is the stability of the printed samples, given that we utilize materials in their partially cured state.[20b,28a,34] To thoroughly evaluate the reliability of these systems, the printed circuits undergo a comprehensive series of assessments. First, multiple samples are printed and placed in a dark environment, with periodic measurements of their conductivity over the course of 40 weeks. As indicated in Figure S6a (Supporting Information), these measurements show that the conductivity experiences negligible changes during this monitoring period. Furthermore, to subject the samples to more extreme conditions, they are exposed to relatively high-intensity UV light from a UV incubator with ≈1.5 mW cm^{-2} power, for 7 weeks period and the conductivity is measured at different time intervals. In addition, the samples are exposed to a full

day of direct sunlight (≈2.5 mW cm^{-2} power in the wavelength 320–475 nm). These conditions are intentionally chosen for their extreme nature, surpassing the harshness of any practical environment in which these samples might be employed. As illustrated in Figures S6b and S7a–c (Supporting Information), the conductivity of the samples exposed to sunlight and 24 h of UV light remains unaltered in comparison to their as-printed counterparts, with the LED diode's light intensity matching that of the initial as-printed sample. However, in the samples subjected to UV light, there is a minor reduction in conductivity after 1 week of exposure, ≈15%, as depicted in Figure S7d,e (Supporting Information). Despite this decrease, these samples continue to effectively illuminate the diode. Notably, the intensities of the UV incubator and sunlight are sufficient for completely curing the resin in less than 30 min when exposed directly. Nevertheless, due to our incorporation of a photo-absorber in the samples, the incident light cannot penetrate into the deep of the sample,[35] where the channels are located, consequently leaving the partially cured resins within the conductive channels unaffected. To evaluate UV light penetration in the samples, Ultraviolet–visible light (UV–vis) analysis was conducted on films with varying grayscale levels (G0, G20, G40, and G60) and thicknesses (50, 100, 150, 200, and 500 µm) with G0 light. The films were fabricated using shim stock placed between two glass slides to achieve the desired thickness. The UV–vis spectra of the 50 µm films with different grayscale levels are shown in Figure S8a (Supporting Information). The results indicate that all films exhibit similar transmittance behavior, as their thickness remains constant, and the concentration of Sudan I, the light-blocking agent, is identical across all grayscale levels. This consistency in absorption is expected since Sudan I effectively blocks UV light, regardless of the grayscale setting.

To further investigate the shielding effect of the G0 material, films of increasing thicknesses (50, 100, 150, 200, and 500 µm) are also analyzed, as shown in Figure S8b (Supporting Information). The results reveal that the 50 µm films absorb ≈70% of UV light (below 530 nm), demonstrating a substantial shielding effect even at this thin layer. As the thickness increases, the transmittance of light continues to decrease, with the 150 µm film showing a significant reduction. Notably, the 200 µm film completely blocks light below 530 nm (≈0% transmittance), confirming that a film as thin as 200 µm provides full protection against UV light, thereby preventing further curing and ensuring the long-term stability of the samples. The effectiveness of Sudan I in blocking UV light is particularly important given that the photoinitiator used in this study has an absorption range of 360–450 nm.[36] This range overlaps with the UV spectrum where Sudan I demonstrates substantial absorption, further highlighting its role in inhibiting curing and ensuring the stability of the films.

It is important to mention that in this experimental setup, the conductive channel (G80) is embedded within a fully cured protective layer (G0), which effectively prevents light penetration due to the presence of Sudan I. This protective layer ensures that the conductive channels remain shielded from UV exposure. Exposure to UV light, or even prolonged ambient light, can induce further polymerization in the partially cured regions, thereby eliminating the conductivity contrast between different parts of the sample. Consequently, when operating in environments where light exposure is inevitable, this issue must be carefully addressed. To mitigate this challenge, the design can be adjusted to ensure that the conductive components are not exposed on the outer surface but are instead encapsulated within fully cured, non-conductive layers . If this approach is not feasible due to design constraints, alternative protective measures, such as the application of UV-blocking sprays, should be considered to maintain the stability of the conductive channels.

Another concern regarding stability is the potential for heat generation in the circuits under electrical current, which could lead to further curing of the partially cured sections and alter their conductivity. To assess this risk, the impact of elevated temperatures on the samples' conductivity is first examined. An embedded channel is printed using G80 resin and the sample is annealed for 6 h at 100 °C. Conductivity measurements are taken in the as-printed state, after 2 h, and after 6 h, as shown in Figure S9a (Supporting Information), revealing no significant change. To further understand thermal polymerization in this system, Differential Scanning Calorimetry (DSC) is conducted. The ink is heated from room temperature to 250 °C at a rate of 5 °C min^{-1}, with the heating cycle presented in Figure S9b (Supporting Information). DSC results indicate that thermal polymerization begins at ≈156 °C. Next, to investigate the practical risk of heat generation under electrical current, samples are subjected to a high voltage of 64 V for 10 h, with their temperatures periodically monitored using an infrared camera. The findings, depicted in Figure S9c,d (Supporting Information), show minimal temperature changes. These results suggest that while the risk of thermal curing exists at high temperatures, the actual temperature of the samples does not increase significantly in practice under the applied voltage conditions due to the minimal heat generated by the electrical current. Thus, the risk of induced reactions and changes in cross-linking due to current-induced heating is negligible.

To ensure the accuracy of our conclusions, we acknowledge that the conductivity of the material remains largely unchanged when it is shielded from light and maintained at room temperature. This approach mitigates the risk of resin curing induced by light exposure or elevated temperatures, which could otherwise invalidate our findings. This technique relies on the contrast in conductivity stemming from different DoC at various sections of the printed object. Resin curing after fabrication would eliminate this contrast, thereby negatively influencing the functionality of the printed objects.

2.4. Small Channel Printing

Next, we investigate the smallest features that can be printed by our method. The pixel size of the DLP setup in this work is 27 µm × 27 µm. Figure S10a (Supporting Information) presents the optical image of the printed samples, wherein the matrix is printed with full light intensity (G0), while in the curved channel region, the light intensity is zero (G100). The deliberate use of zero light intensity in this context serves the purpose of maintaining the resin in an uncured state within that particular area. Subsequently, the uncured resin can be effectively washed-out post-printing, yielding a carved pattern, which can be visually observed. The width of this channel is ≈100 µm.

In Figure S10b (Supporting Information), the modulus map of the thin channel within the fully cured matrix is illustrated, derived from nanoindentation analysis. The light intensities employed for curing the channel and the bulk, denoted as G60 and G0, respectively, yield distinct mechanical properties (Figure 2f). Both G60 and G0 yield solid polymers, therefore the analysis surface for nanoindentation is flat, whereas their properties are different. Notably, this map reveals the successful printing of high-resolution features, with widths as diminutive as 100 µm. Figure S10c (Supporting Information) further demonstrates the contrast in mechanical properties of these regions by presenting the corresponding load-depth curve. These results highlight our adeptness in manipulating resolution and fabricating small-scale features with varying conductivities. Such proficiency holds great promise as an agile tool in advancing microelectronics fabrication techniques. As illustrated here, the primary constraint in achieving even finer structures lies in the resolution of the projector utilized. By employing more advanced and higher-resolution projectors, we can push the boundaries of resolution further, enabling the creation of even more intricate structures with superior precision and detail.

2.5. g-DLP 3D Printing of Sensors

As shown in Figure 2c, within the solid-state region (≤G60), the conductivity of the samples changes with variations in light intensity. Notably, even within the solid state, materials denoted as G0 and G60 display conductivity levels that differ by ~20-fold. This conductivity gradient serves as a good leverage, enabling the rapid development of sensors for diverse applications. **Figure 5**a illustrates a simple design for a sensor capable of detecting of placing force on the middle of the top part, suitable for various applications like switches and pressure sensors. This design juxtaposes low-conductivity G0 regions with high-conductivity G60 regions, using G60 for the yellow sections while interspersing them with G0 portions in blue. The G0 columns in this design act as insulators between the more conductive G60 plates. By putting this sensor in a series circuit via attaching the G60 sheets to the two ends of the circuit and consequently pressing the middle (Figure 5b), the contact between the conductive sheets leads to a change in resistance, enabling the detection of pressure on the sensor. This change occurs upon contact between the plates with G60's higher conductivity. The sensor's stability and responsiveness are assessed by cyclically pressing the middle and monitoring resistance, with results displayed in Figure 5c, showing consistent stability across more than 500 cycles. This sensor is printed in ~15 min. A movie of this sensor is presented in Movie S2 (Supporting Information).

We then fabricate a flex sensor, achieving a fast-printing time of just 6 min (Figure 5d). The sensor comprises two distinct grayscale elements, G60 and G0, with two discrete G60 sections superimposed onto a continuous G0 sheet. In its initial state, when straight, the sensor has high resistance. As the sample bends, the two G60 plates come into contact, resulting in a sudden and substantial drop in resistance. When affixed to a finger, the sensor adeptly captures the bending motion, offering a straightforward and effective means of detection (Figure 5e). Figure 5f illustrates the representation of the resistance change data from this sensor. Notably, it shows the sensor's capability to yield stable signals, as well as high gauge factor (≈80%). A movie of this sensor demonstrating its responsiveness is presented in Movie S3 (Supporting Information).

The adaptability of this sensor extends to its customizable sensitivity to bending, a feature regulated by manipulating the gap size between the G60 plates. In essence, the sensor's responsiveness to bending forces is intricately tied to the dimensions of this gap—specifically, a smaller gap imparts heightened sensitivity. This nuanced control over sensitivity provides a practical means of tailoring the sensor's performance to distinct application requirements, underscoring its versatility and potential for finely tuned applications in various fields.

Illustrating this potential, Figure 5g shows a sensor employing three distinct grayscales, aiming to detect various degrees of bending. This design, the modified version of the sensor depicted in Figure 5d, features a continuous G0 sheet at the base, with G50 and G60 plates superimposed over it. Notably, the gap between the G60 plates, characterized by higher conductivity, is intentionally larger than that between the G50 plates, achieved by incorporating a slight slope on one side. This sensor design can detect different bending angles. As shown in Figure 5h, bending to a certain degree (half-bend) causes contact between the G50 plates, yielding a detectable change in resistance. Further bending (full-bending) results in contact between the G60 plates, producing a more pronounced signal. Figure 5i demonstrate the resistance change of this sensor in two different bending rhythms. It can be observed that this simple sensor is very responsive to bending degree, with 90% $\Delta R/R_0$ for full bend and 60% $\Delta R/R_0$ for half bend. The contrast between two signals is high enough to be detected easily and incorporated for different applications. It is worth noting that owing to the capabilities of g-DLP technique this upgrade from the sensor in Figure 5d is achieved through manipulating of the slides, yielding same printing time but more complexity and functionality.

Next, we demonstrate printing of a complex yet fully functional sensor by integrating multiple parts printed with different grayscale Illustrated in Figure 5j,k are the model design for a joystick, employing five distinct grayscales: G0, G45, G50, G55, and G60. The design features a moving handle printed with the G55 grayscale, surrounded by four columns, each characterized by different conductivity properties. A separator, printed with maximum light intensity (G0), functions as an insulator, demarcating the handle from the surrounding structure. Making a circuit through the connection between the handle and the bottom part results in the successful creation of a sensor. The movement of the handle in various directions initiates contact with different columns, inducing a discernible drop in resistance. The resulting $\Delta R/R$ graph, as depicted in Figure 5l, the distinct and easily distinguishable signal intensities for each directional movement. This fully functional sensor is manufactured within a 40 min printing duration. A movie of this sensor is presented in Movie S4 (Supporting Information).

By leveraging the capabilities arising from the combination of materials and techniques, we design more complex electronics. As depicted in **Figure 6**a. we design a sensor comprising two grayscales (G0 and G60). This sensor features two parallel G60 plates that do not have contact with each other and are separated

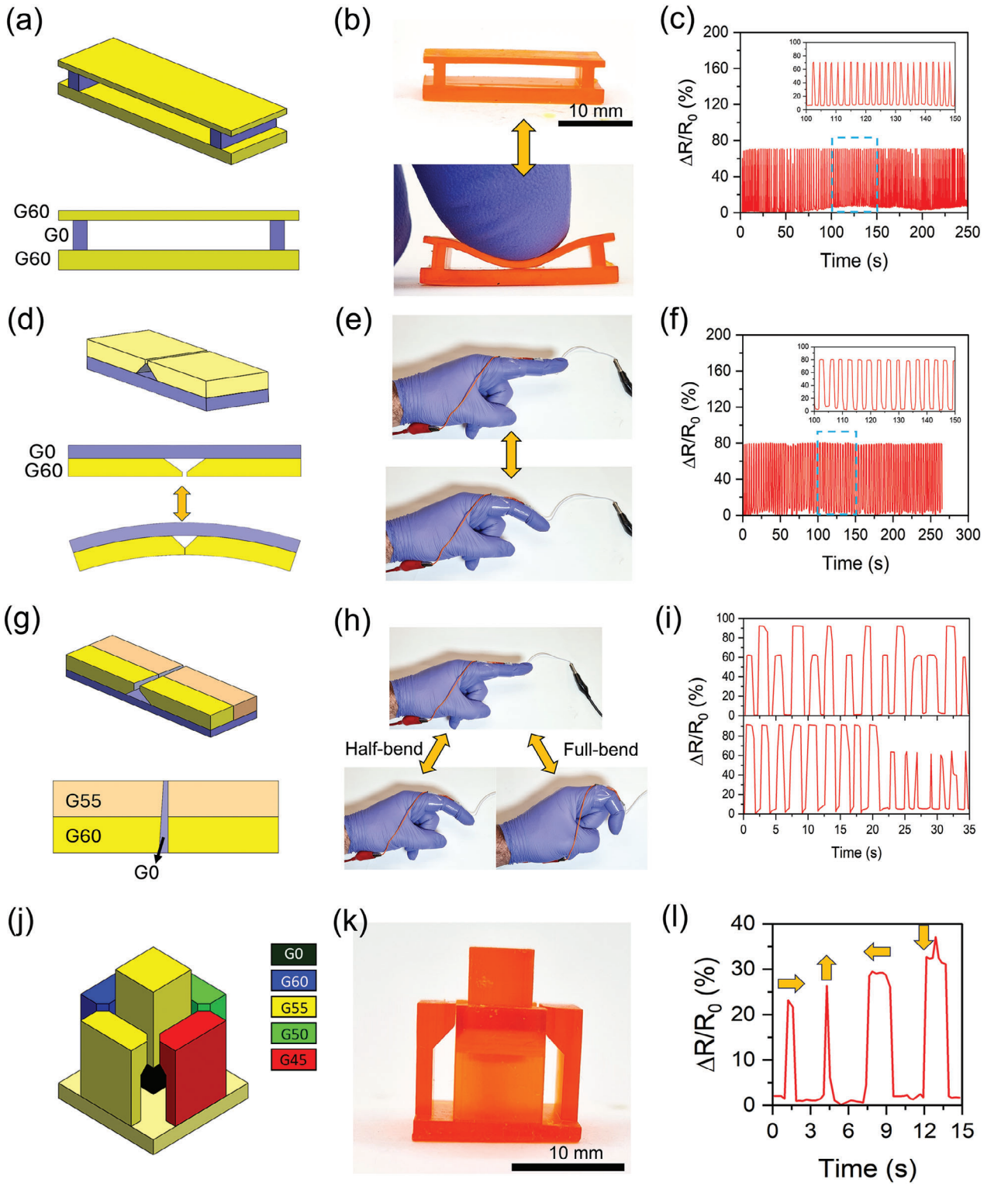

Figure 5. Printing mechanical sensors. a) the schematic illustration of the simple sensor that made of two different grayscale (G0 and G60) to detect mechanical force. b) image of the sensor, that by placing a finger at the midle, the G60 plates at the bottom and top connect and provide a signal. c) the ΔR/R0 graph for this sensor. d) the schematic illustration of the simple bending sensor. e) attaching the sensor to index figure and monitor the resistance, f) the corresponding ΔR/R0 graph for this sensor g) The schematic illustration of the flex sensor with capability of detecting 2 degrees of bending, h) attaching the sensor to index figure and monitor the resistance, i) the corresponding ΔR/R0 for the bending sensor, with distinguishable signals in the resistance resulting from the half- and full-bending motions. j) schematic illustration and k) the image of the simple joystick designed to detect the motion in different directions, and l) the corresponding ΔR/R0 for joystick moved in different directions.

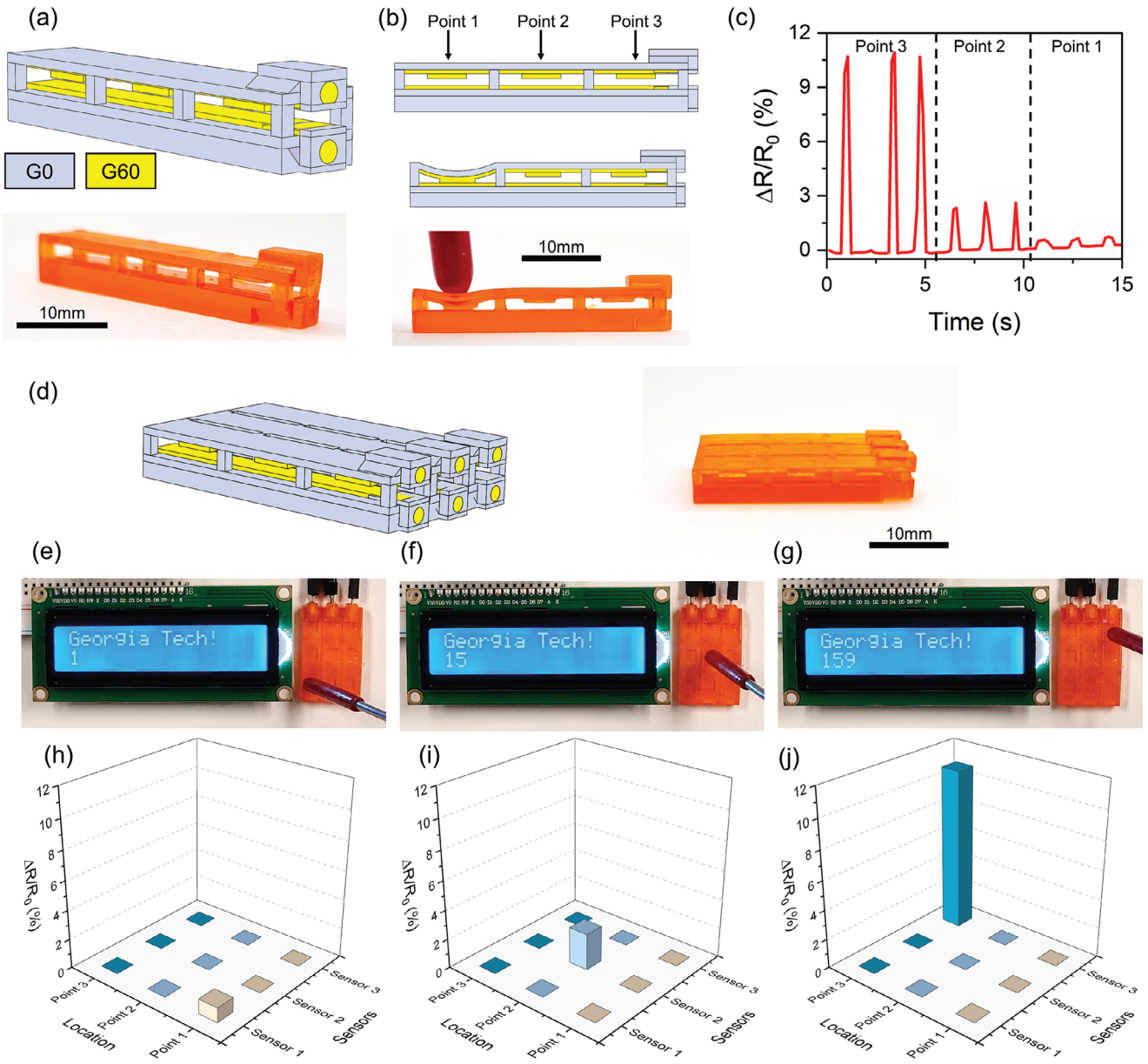

Figure 6. Design and fabrication of a keyboard. a) Schematic illustration and the image of the 3 × 1 key sensor, b) the conduction mechanism of the sensor by closing the circuits with different length due to pressing different regions, c) $\Delta R/R_0$ response corresponding to different points of the sensor, d) schematic illustration and image of the 3 × 3 mini keyboard, e–h) response behaviors of the printed keyboard when placing force on the keys, and h–j) corresponding $\Delta R/R_0$ for the keyboard in different keys.

by the rest of the structure, printed with maximum light intensity. Applying force to different locations on this sensor closes the circuit by connecting the G60 plates. We design three points, each capable of closing the circuit with different lengths based on their distance from the connecting point at one end (Figure 6b). Consequently, different signals are produced. The weakest signal corresponds to point 1, with the longest circuit, while pressing point 3 closes the circuit with the shortest length, producing the strongest signal among these three points (Figure 6c). The gauge factors for these three points are 1, 3, and 11%, which is enough to be distinguished and consequently monitor the force location.

Next, three of these sensors are combined to fabricate a 3 × 3 mini keyboard. The model and fabricated sensor are presented in Figure 6d. This sensor is printed in just 30 min. We use an Arduino microcontroller to read the resistance data and translate the information into an LCD display. The circuit is designed to translate each key to a number from 1 to 9 (bottom-left corresponds to number 1, and the top-right key corresponds to number 9). The image of the full circuit and its schematic are presented in Figures S11 and S12 (Supporting Information), respectively. Figure 6e–g shows snapshots of this keyboard and LCD, along with the corresponding graphs for R for each point

in Figure 6h–j. It can be observed that these distinguishable signals in resistance enable us to fabricate a complex and functional keyboard. A movie of this sensor is presented in Movie S5 (Supporting Information).

3. Conclusion

In this study we develop a novel resin for g-DLP 3D printing that enables us to fabricate electronics with significant differences in their conductivity in a single-vat single-cure 3D printing process. In the g-DLP process, low light intensity yields low monomer conversion with the glass transition below 0 °C. Conversely, under maximum light intensity, the structure undergoes complete curing and exhibits glassy properties at room temperature. Lithium salt is added to enable conductivity. In the sample with low light intensity, it contains uncured or partially cured monomers, facilitating ion movement and thus provide high conductivity. In samples with high light intensity, the fully cured samples in the glassy state limits ion mobility, resulting in significantly reduced conductivity. Using this strategy, we are able to print samples with conductivity in range of 2×10^{-2} to 1×10^{-5} S m^{-1}, almost 2000 times different. The synergy between g-DLP and this intentionally designed ink offers a straightforward single-vat method for fabricating electronics with integrated components featuring differing conductivity levels. The versatility of g-DLP technique in combination of our designed ink is demonstrated through printing of circuits with simple and complex geometries as well as different functional sensors (bending sensors, a simple switch-like sensor, a joy-stick like sensor, and a mini keyboard). Although these parts contain partially cured polymers in their structure, by proper design and embedding the partially cured polymers in the matrix of fully cured polymers, the object are remarkably stable for weeks, even under harsh conditions. The printing process for making fully functional electronics is fast, some sensor can be printed in several minutes. This work introduces a rapid technique for manufacturing soft electronics suitable for various applications, providing an effective solution for prototyping and performance validation.

4. Experimental Section

Materials: The composition of the photocurable resin in this investigation was achieved by mixing PEGDA (Mn = 250), GMA, AUD (Ebecryl 8413), with a weight ratio of 70:25:5, respectively. Two alternative inks were used for evaluation of expandability of this technique to include i) BA, PEGDA (Mn = 250) and Ebecryl 8413 with a weight ratio of 45:45:10 respectively, and ii) 2-HEA and BPAEDA (Mn = 512) with weigh ratio of 80:20, respectively. In addition, the ink includes 1 wt% of photoinitiator (Irgacure 819) and 0.1 wt% photo absorber (Sudan I). LiTFSI was used as a source of conductivity, which was soluble in the photocurable resin up to 60 wt%. All of the above chemical except Ebecryl 8413 that was provided by Allnex (Alpharetta, GA, USA) were purchased from Sigma-Aldrich (St. Louis, MO, USA) and used as received.

Safety Guidelines: Acrylate-based monomers, particularly GMA, pose significant safety hazards due to their potential for skin sensitization, irritation, and other toxic effects, necessitating careful handling procedures including the use of personal protective equipment (PPE), proper ventilation, and strict adherence to safety protocols to minimize exposure. In this study, varying degrees of curing were employed to achieve different levels of conductivity across the sample. In regions with lower monomer conversion, residual monomer might be present, which, depending on the sample design, might be on the surface. Therefore, it is highly recommended to take necessary precautions when working with this chemical and to carefully read the Safety Data Sheet (SDS) before use and handling.

3D Printing: 3D printing was performed with a bottom-up DLP printer that employs a 385 nm UV-LED light projector (PRO4500, Wintech Digital Systems Technology Corp., Carlsbad, CA, USA) and a linear translation stage (LTS150 Thorlabs, Newton, NJ, USA). A homemade container with an oxygen-permeable window (Teflon AF-2400, Vici Metronics Inc., Poulsbo, WA, USA) was used as the resin vat. The designed 3D structures were sliced into image files with a thickness of 0.05 mm and then converted into grayscaled image files with a MATLAB script. The layer-by-layer approach was utilized at the optimized speed of 3 s per layer to print the designed 3D structures. All samples were raised with isopropyl alcohol after printing. The light intensity of the printer was calibrated with a photometer (ILT1400-A Radiometer, International Light Technologies Inc., MA, USA) before printing.

Properties Characterization: The uniaxial tension tests were performed with a universal test machine (Insight 10, MTS Systems Corp., Eden Prairie, MN, USA) with a cross-head speed of 5 mm min^{-1}. Dynamic thermomechanical properties were conducted on a DMA machine (Q800, TA Instruments, New Castle, DE, USA) with a temperature ramped at a rate of 2 °C min^{-1}. DMA analysis was conducted at frequency of 1 Hz and a strain of 0.1%.[37] The degree of curing was decided by normalized FTIR (Nicolet iS50 spectrometer, Thermo Fisher Scientific, Waltham, MA, USA) peak intensity of the acrylate group present at 809 cm^{-1}. Multiple tests were conducted for each sample to guarantee reproducibility. DSC analyses were measured on a DSC system (Discovery DSC 250, TA Instruments, New Castle, DE, USA) with heating rate of 5 °C min^{-1} from room temperature to 250 °C. UV–vis spectra of the samples in different grayscale were obtained using an Ultrospec 2100 pro UV–visible Spectrophotometer (Amersham Biosciences, Amersham, United Kingdom) from printed films samples with thickness of ≈0.5 mm. The data collected in range of 250–900 nm wavelength in transmittance mode.

Characterization of Conductivity: The conductivity of the samples was calculated by $\sigma = L/(SR)$, where L is the distance between the electrodes, S is the cross sectional area of the sample, and R is the bulk resistance and is measured by the multimeter. The bulk resistance of the samples was measured by a Keithley 2100 Series: 6.5 Digit USB Multimeter. When measuring the resistance of materials with ionic conductivity using DC methods, a charge accumulation phenomenon occurs, as demonstrated in Figure S13 (Supporting Information). This phenomenon causes the resistance to increase over time. However, the resistance eventually reaches a stable plateau after several minutes. To account for this effect, all resistance measurements using a multimeter include a 10 min waiting time before data recording. This waiting time mitigates the initial charge accumulation effects, ensuring more consistent and accurate conductivity measurements. To prevent any monomer leakage during the measurement of these samples in their liquid state, the electrodes were glued and sealed to the ends of the channels. This ensures proper sealing, minimizing safety concerns related to acrylate-based monomers and improving the stability of the sample's conductivity by preventing monomer evaporation. To conduct conductivity measurements on solid samples at lower grayscale, a four-point probe technique was employed on printed films with a thickness of 0.5 mm, utilizing the sheet resistance measurement system (Ossila, Sheffield, UK).

MD Simulation: Classical MD simulations were conducted to validate experimental observations across the spectrum of curing percentages. All simulations were conducted on systems of the same composition as the ink used for DLP 3D printing process. Initially, cross-linking were simulated using a modified version of the HTPolyNet[38] algorithm, which iteratively cross-links an initial system of randomly distributed GMA monomers with AUD and PEGDA. To reduce the computational costs needed for curing, a small system of 1000 atoms was first cross-linked. Multiple replicates of the small systems were then combined inside a simulation box to reach the target atom count to perform the property calculations. All systems were energy minimized, heated and equilibrated to have a similar density to the experimental samples at the normal temperature

and pressure. The general AMBER force field (GAFF2) was used for the molecular interactions of the polymer network.

The glass transition temperature, T_g is calculated using a ≈12000 atoms system by measuring the density as it is cooled. Simulated annealing in an NPT ensemble was performed for a total of 5 ns at the reference temperatures of 500, 300, 700, 300, 700, and 500 K to equilibrate the system. Finally, for Tg simulations, the annealed system was started at 500 K and was cooled at intervals of 20 K until 80 K. Each cooling interval consist of an NPT stage for 0.5 ns, an NVT equilibrium for 0.5 ns, and an NPT production run which measured the density of the system. A bilinear fitting protocol was used to find the T_g value.[39]

The lithium ions conductivity was calculated in a ≈4000 atoms system. First, the cross-linked system was equilibrated to reach the experimental density. Next, 20 LiTFSI pairs corresponding to 20 wt% were randomly added around the polymer network. GAFF2 compatible parameters developed by Aqvist[40] and a charge scaling of 0.8 were used for simulating the lithium ions in the non-aqueous environment. AM1-BCC charges and GAFF2 parameters were calculated generated using AmberTools[41] and used for the TFSI- ions. After adding the ions, the system was energy minimized and heated to 300 K in an NVT ensemble for 300 ps. An NPT equilibration run at 7.0 atm, 300 K for 15,000 ps was used to ensure that lithium ions and TFSI- diffused inside the polymer network. Finally, an NVT production run for 100 ns at 300 K was conducted, and the Mean Square Displacement (MSD) of the lithium ions across time were measured. A linear fit of MSD versus time gives the self-diffusion (D_s) from Equation (1),[42]

$$D_s = \lim_{t\to\infty} \frac{1}{6Nt} \sum_{i=1}^{N} \left\langle (\Delta \boldsymbol{r}_i(t))^2 \right\rangle \quad (1)$$

where t is time, N is the number of lithium ions, and $\Delta \boldsymbol{r}_i(t)$ is the displacement of ion i at time t. D_s is then used in the Einstein-Nernst Equation to calculate the ionic conductivity[5] using the Equation (2),

$$\sigma = \frac{ne^2Z^2}{k_D T} D_s \quad (2)$$

where n is ion number density in ions/cm^3, e is the charge of an electron, Z is the valence of lithium ions, k_D is the Boltzmann constant, T is the temperature. For each of the 3 polymer systems, 2 additional trials with different initial positions of ions were used to calculate the conductivity. The mean and standard deviation of all 6 trials were calculated for the datapoint.

Supporting Information

Supporting Information is available from the Wiley Online Library or from the author.

Acknowledgements

The support from an AFOSR grant (FA9550-20-1-0306; Dr. B.-L. "Les" Lee, Program Manager) and an NSF grant (CMMI-2323695) are gratefully acknowledged. The authors want to thank Dr. V. Varshney of AFRL for helpful discussions regarding the MD simulation system.

Conflict of Interest

The authors declare no conflict of interest.

Data Availability Statement

The data that support the findings of this study are available in the supplementary material of this article.

Keywords

3D printing, Conductivity, g-DLP, Soft electronics

Received: June 19, 2024
Revised: September 15, 2024
Published online: September 28, 2024

[1] C. J. Lee, H. Wu, Y. Hu, M. Young, H. Wang, D. Lynch, F. Xu, H. Cong, G. Cheng, *ACS Appl. Mater. Interfaces* **2018**, *10*, 5845.
[2] K. Namsheer, C. S. Rout, *RSC Adv.* **2021**, *11*, 5659.
[3] T.-T. Le, M. Abbas, D. M. Dreistadt, T. Klassen, C. Pistidda, *Chem. Eng. J.* **2023**, *473*, 145315.
[4] Y. Fan, X. Wang, X. Zhang, Z. Chang, W. Kuang, H. Tian, *ACS Appl. Polym. Mater.* **2023**, *5*, 8430.
[5] W. Zhou, Y. Jiang, Q. Xu, L. Chen, H. Qiao, Y.-X. Wang, J.-C. Lai, D. Zhong, Y. Zhang, W. Li, Y. Du, X. Wang, J. Lei, G. Dong, X. Guan, S. Ma, P. Kang, L. Yuan, M. Zhang, J. B. H. Tok, D. Li, Z. Bao, W. Jia, *Nat. Biomed. Eng.* **2023**, *7*, 1270.
[6] a) M. Criado-Gonzalez, A. Dominguez-Alfaro, N. Lopez-Larrea, N. Alegret, D. Mecerreyes, *ACS Appl. Polym. Mater.* **2021**, *3*, 2865; b) X. He, J. Cheng, Z. Li, H. Ye, Z. Sun, Q. Liu, H. Li, R. Wang, Q. Ge, *Adv. Mater. Technol.* **2023**, *8*, 2202088; c) H. Yuk, B. Lu, S. Lin, K. Qu, J. Xu, J. Luo, X. Zhao, *Nat. Commun.* **2020**, *11*, 1604.
[7] a) M. Criado-Gonzalez, A. Dominguez-Alfaro, N. Lopez-Larrea, N. Alegret, D. Mecerreyes, *ACS Appl. Polym. Mater.* **2021**, *3*, 2865; b) I. M. Hill, V. Hernandez, B. Xu, J. A. Piceno, J. Misiaszek, A. Giglio, E. Junez, J. Chen, P. D. Ashby, R. S. Jordan, Y. Wang, *ACS Appl. Polym. Mater.* **2023**, *5*, 3989; c) S. Ghaderi, H. Hosseini, S. A. Haddadi, M. Kamkar, M. Arjmand, *J. Mater. Chem. A* **2023**, *11*, 16027.
[8] a) S. Hao, C. Shao, L. Meng, C. Cui, F. Xu, J. Yang, *ACS Appl. Mater. Interfaces* **2020**, *12*, 56509; b) A. Navaei, H. Saini, W. Christenson, R. T. Sullivan, R. Ros, M. Nikkhah, *Acta Biomater.* **2016**, *41*, 133.
[9] a) B. Zhu, E. W. C. Chan, S. Y. Li, X. Sun, J. Travas-Sejdic, *J. Mater. Chem. C* **2022**, *10*, 14882; b) L. Zhao, X. Li, Y. Li, X. Wang, W. Yang, J. Ren, *Biomacromolecules* **2021**, *22*, 1273.
[10] a) L.-Y. Hsiao, L. Jing, K. Li, H. Yang, Y. Li, P.-Y. Chen, *Carbon* **2020**, *161*, 784; b) J. Tropp, C. P. Collins, X. Xie, R. E. Daso, A. S. Mehta, S. P. Patel, M. M. Reddy, S. E. Levin, C. Sun, J. Rivnay, *Adv. Mater.* **2024**, *36*, 2306691; c) L. Mottet, D. L. Cornec, J.-M. Noël, F. Kanoufi, B. Delord, P. Poulin, J. Bibette, N. Bremond, *Soft Matter* **2018**, *14*, 1434.
[11] a) H. He, J. Ouyang, *Acc. Mater. Res.* **2020**, *1*, 146; b) P. Li, K. Sun, J. Ouyang, *ACS Appl. Mater. Interfaces* **2015**, *7*, 18415.
[12] C. Kant, S. Mahmood, M. Seetharaman, M. Katiyar, *Small Methods* **2023**, *8*, 2300638.
[13] Y. Khan, F. J. Pavinatto, M. C. Lin, A. Liao, S. L. Swisher, K. Mann, V. Subramanian, M. M. Maharbiz, A. C. Arias, *Adv. Funct. Mater.* **2016**, *26*, 1004.
[14] L.-W. Lo, J. Zhao, H. Wan, Y. Wang, S. Chakrabartty, C. Wang, *ACS Appl. Mater. Interfaces* **2021**, *13*, 21693.
[15] B. Weng, A. Morrin, R. Shepherd, K. Crowley, A. J. Killard, P. C. Innis, G. G. Wallace, *J. Mater. Chem. B* **2014**, *2*, 793.
[16] J. Persad, S. Rocke, *Results Eng.* **2022**, *16*, 100730.
[17] a) H. He, R. Chen, S. Yue, S. Yu, J. Wei, J. Ouyang, *Sci. Adv.* **2022**, *8*, abq8160; b) U. Lang, N. Naujoks, J. Dual, *Synth. Met.* **2009**, *159*, 473.
[18] D. J. Roach, C. M. Hamel, C. K. Dunn, M. V. Johnson, X. Kuang, H. J. Qi, *Addit. Manuf.* **2019**, *29*, 100819.
[19] X. Fan, W. Nie, H. Tsai, N. Wang, H. Huang, Y. Cheng, R. Wen, L. Ma, F. Yan, Y. Xia, *Adv. Sci.* **2019**, *6*, 1900813.
[20] a) L. Yue, X. Sun, L. Yu, M. Li, S. M. Montgomery, Y. Song, T. Nomura, M. Tanaka, H. J. Qi, *Nat. Commun.* **2023**, *14*, 5519; b) L. Yue, S.

Macrae Montgomery, X. Sun, L. Yu, Y. Song, T. Nomura, M. Tanaka, H. Jerry Qi, *Nat. Commun.* **2023**, *14*, 1251.
[21] a) Q. Yu, Z. Zhu, X. Fan, D. Wang, presented at *International Conference on* Intelligent Robotics and Applications, Singapore, October **2023**; b) X. Peng, X. Kuang, D. J. Roach, Y. Wang, C. M. Hamel, C. Lu, H. J. Qi, *Addit. Manuf.* **2021**, *40*, 101911; c) E. A. Guzzi, R. Bischof, D. Dranseikiene, D. V. Deshmukh, A. Wahlsten, G. Bovone, S. Bernhard, M. W. Tibbitt, *Biofabrication* **2021**, *13*, 044105.
[22] S. Park, W. Shou, L. Makatura, W. Matusik, K. Fu, *Matter* **2022**, *5*, 43.
[23] a) V. G. Rocha, E. Saiz, I. S. Tirichenko, E. García-Tuñón, *J. Mater. Chem. A* **2020**, *8*, 15646; b) A. Khan, K. Rahman, S. Ali, S. Khan, B. Wang, A. Bermak, *J. Mater. Res.* **2021**, *36*, 3568.
[24] S. G. M. Uzel, R. D. Weeks, M. Eriksson, D. Kokkinis, J. A. Lewis, *Adv. Mater. Technol.* **2022**, *7*, 2101710.
[25] Q. Mu, L. Wang, C. K. Dunn, X. Kuang, F. Duan, Z. Zhang, H. J. Qi, T. Wang, *Addit. Manuf.* **2017**, *18*, 74.
[26] U. Shaukat, E. Rossegger, S. Schlögl, *Polymers* **2021**, *231*, 124110.
[27] a) F. Zhang, L. Zhu, Z. Li, S. Wang, J. Shi, W. Tang, N. Li, J. Yang, *Addit. Manuf.* **2021**, *48*, 102423; b) H.-J. Hsu, S.-Y. Lee, C.-P. Jiang, *Int. J. Autom. Smart Technol.* **2018**, *8*, 173.
[28] a) X. Kuang, J. Wu, K. Chen, Z. Zhao, Z. Ding, F. Hu, D. Fang, H. J. Qi, *Sci. Adv.* **2019**, *5*, aav5790; b) M. Zhang, X. Fan, L. Dong, C. Jiang, O. Weeger, K. Zhou, D. Wang, *Adv. Sci.* **2024**, *11*, 2309932; c) B. Zhao, M. Zhang, L. Dong, D. Wang, *Composites Commun.* **2022**, *36*, 101395.
[29] X. Peng, L. Yue, S. Liang, S. Montgomery, C. Lu, C.-M. Cheng, R. Beyah, R. R. Zhao, H. J. Qi, *Adv. Funct. Mater.* **2022**, *32*, 2112329.
[30] J. Zhang, Q. Hu, S. Wang, J. Tao, M. Gou, *Int. J. Bioprint.* **2020**, *6*, 242.
[31] a) N. Tanibata, R. Morimoto, K. Nishikawa, H. Takeda, M. Nakayama, *Anal. Chem.* **2020**, *92*, 3499; b) X.-X. Zhang, M. Liang, N. P. Ernsting, M. Maroncelli, *J. Phys. Chem. Lett.* **2013**, *4*, 1205; c) K. L. Gering, *Electrochim. Acta* **2017**, *225*, 175; d) A. V. Marenich, C. J. Cramer, D. G. Truhlar, *J. Phys. Chem. B* **2009**, *113*, 6378.
[32] a) Z. Stoeva, I. Martin-Litas, E. Staunton, Y. G. Andreev, P. G. Bruce, *J. Am. Chem. Soc.* **2003**, *125*, 4619; b) G. S. MacGlashan, Y. G. Andreev, P. G. Bruce, *Nature* **1999**, *398*, 792; c) S. Mogurampelly, V. Ganesan, *Macromolecules* **2015**, *48*, 2773.
[33] a) X. He, J. Cheng, Z. Li, H. Ye, Z. Sun, Q. Liu, H. Li, R. Wang, Q. Ge, *Adv. Mater. Technol.* **2023**, *8*, 2202088; b) M. T. H. Nguyen, S. Y. Kim, T. H. Jeong, J. H. Kim, H. S. Cho, T. H. Ha, S. J. Ahn, Y. H. Kim, *Electron. Mater. Lett.* **2022**, *18*, 275; c) Y. Zheng, X. Huang, J. Chen, K. Wu, J. Wang, X. Zhang, *Materials* **2021**, *14*, 3911.
[34] a) Z. Chen, M. Yang, M. Ji, X. Kuang, H. J. Qi, T. Wang, *Mater. Des.* **2021**, *197*, 109189; b) C. T. Forte, S. M. Montgomery, L. Yue, C. M. Hamel, H. J. Qi, *J. Appl. Mech.* **2023**, *90*, 071003.
[35] a) C. S. Ng, A. S. Subramanian, P.-C. Su, *Addit. Manuf.* **2022**, *59*, 103118; b) A. Salas, M. Zanatta, V. Sans, I. Roppolo, *ChemTexts* **2023**, *9*, 4.
[36] S. Jradi, L. Balan, X. H. Zeng, J. Plain, D. J. Lougnot, P. Royer, R. Bachelot, S. Akil, O. Soppera, L. Vidal, *Nanotechnology* **2010**, *21*, 095605.
[37] a) Y. Ding, R. Miao, J. Liu, Z. Xin, C. Bao, *ACS Appl. Polym. Mater.* **2024**, *6*, 9008; b) L. Yue, Y.-L. Su, M. Li, L. Yu, S. M. Montgomery, X. Sun, M. G. Finn, W. R. Gutekunst, R. Ramprasad, H. J. Qi, *Adv. Mater.* **2023**, *35*, 2300954; c) S. Wang, Y. Ma, Z. Deng, S. Zhang, J. Cai, *Polym. Test.* **2020**, *86*, 106483; d) M. Li, F. Gholami, L. Yue, M. R. Fratarcangeli, E. Black, S. Shimokawa, T. Nomura, M. Tanaka, H. Kobayashi, Y. Song, H. J. Qi, *Adv. Funct. Mater.* **2024**, 2406847.
[38] M. Huang, C. F. Abrams, *SoftwareX* **2023**, *21*, 101303.
[39] M. A. F. Afzal, A. R. Browning, A. Goldberg, M. D. Halls, J. L. Gavartin, T. Morisato, T. F. Hughes, D. J. Giesen, J. E. Goose, *ACS Appl. Polym. Mater.* **2021**, *3*, 620.
[40] J. Àqvist, *J. Phys. Chem.* **1990**, *94*, 8021.
[41] D. A. Case, H. M. Aktulga, K. Belfon, D. S. Cerutti, G. A. Cisneros, V. W. D. Cruzeiro, N. Forouzesh, T. J. Giese, A. W. Götz, H. Gohlke, S. Izadi, K. Kasavajhala, M. C. Kaymak, E. King, T. Kurtzman, T.-S. Lee, P. Li, J. Liu, T. Luchko, R. Luo, M. Manathunga, M. R. Machado, H. M. Nguyen, K. A. O'Hearn, A. V. Onufriev, F. Pan, S. Pantano, R. Qi, A. Rahnamoun, A. Risheh, et al., *J. Chem. Inf. Model.* **2023**, *63*, 6183.
[42] A. Baktash, J. C. Reid, T. Roman, D. J. Searles, *npj Comput. Mater.* **2020**, *6*, 162.